

# Advanced Alkali Treatments for High-Efficiency Cu(In,Ga)Se<sub>2</sub> Solar Cells on Flexible Substrates


Romain Carron,\* Shiro Nishiwaki, Thomas Feurer, Ramis Hertwig, Enrico Avancini, Johannes Löckinger, Shih-Chi Yang, Stephan Buecheler, and Ayodhya N. Tiwari

Flexible, lightweight Cu(In,Ga)Se<sub>2</sub> (CIGS) solar cells grown on polymer substrates are a promising technology with fast growing market prospects. However, power conversion efficiencies of solar cells grown at low temperatures ( $\approx 450^\circ\text{C}$ ) remain below the efficiencies of cells grown at high temperature on glass substrates. This contribution discusses the impact on cell efficiency of process improvements of low-temperature CIGS deposition on flexible polyimide and glass substrates. Different strategies for incorporation of alkali elements into CIGS are evaluated based on a large number of depositions. Postdeposition treatment with heavy alkali (here RbF) enables a thickness reduction of the CdS buffer layer and increases the open-circuit voltage. Na supply during 3rd stage CIGS deposition positively impacts the cell performance. Coevaporation of heavy alkali (e.g., RbF) during capping layer deposition mitigates the adverse shunting associated with high Cu contents, yielding highest efficiencies with near-stoichiometric absorber compositions. Furthermore, optimization of the deposition sequence results in absorbers with a  $1\ \mu\text{m}$  wide notch region with nearly constant bandgap minimum. The improved processes result in a record cell efficiency of 20.8% for CIGS on flexible substrate.

## 1. Introduction

Thin-film Cu(In,Ga)Se<sub>2</sub> (CIGS) solar cells can be manufactured as flexible and lightweight devices utilizing roll-to-roll or sheet-to-sheet production techniques.<sup>[1]</sup> In addition to cost-reduction and aesthetic considerations, flexible photovoltaic (PV) devices with adjustable form factors open new opportunities in fast-growing markets such as building integration, portable electronics, mobility applications as well as aerospace.<sup>[2]</sup>

Dr. R. Carron, Dr. S. Nishiwaki, T. Feurer, R. Hertwig, E. Avancini, J. Löckinger, S.-C. Yang, Dr. S. Buecheler, Prof. A. N. Tiwari  
Laboratory for Thin Films and Photovoltaics  
Empa – Swiss Federal Laboratories for Materials Science and Technology  
Überlandstrasse 129, CH-8600 Dübendorf, Switzerland  
E-mail: romain.carron@empa.ch

 The ORCID identification number(s) for the author(s) of this article can be found under <https://doi.org/10.1002/aenm.201900408>.

© 2019 The Authors. Published by WILEY-VCH Verlag GmbH & Co. KGaA, Weinheim. This is an open access article under the terms of the Creative Commons Attribution-NonCommercial License, which permits use, distribution and reproduction in any medium, provided the original work is properly cited and is not used for commercial purposes.

The copyright line for this article was changed on 26 September 2019 after original online publication.

DOI: 10.1002/aenm.201900408

Manufacturing of flexible CIGS solar modules polyimide (PI) substrates requires low temperature deposition resulting in lower efficiencies<sup>[3]</sup> as compared to devices processed at high temperature on glass substrate.<sup>[4–6]</sup> Recent progresses in the field of low-temperature CIGS were enabled by absorber treatments with heavy alkali compounds.<sup>[3,7]</sup> In this contribution, we aim at reducing this efficiency gap by refining the CIGS manufacturing processes, by adjusting the Cu concentration and Ga gradient in the absorber, and by investigating different strategies for alkali incorporation.

### 1.1. CIGS Absorber Composition

CIGS efficiency records were historically achieved with low Cu contents, defined with the compositional ratio CGI  $[\text{Cu}]/([\text{Ga}]+[\text{In}])$  in the range of 0.8–0.9 (ref. [8] and references therein). CIGS is

surprisingly tolerant to Cu-deficient compositions, as notably investigated numerically by the group of Zunger.<sup>[9,10]</sup> Multiple reasons motivate an increase of the Cu content toward stoichiometry: lower Urbach energies indicating lesser amplitude of potential fluctuations, lower defect density, and improved transport<sup>[11]</sup> or increased optical absorption.<sup>[12,13]</sup> CIGS layers presenting a degree of Cu excess also exhibit improved crystallinity<sup>[14]</sup> and sharper photoluminescence (PL) spectra.<sup>[15]</sup> However, CIGS cells with increased Cu contents generally do not yield the expected PV performance<sup>[16,17]</sup> notably due to formation of Cu<sub>x</sub>Se secondary phases in the surface region, recent experiments open processing routes for stoichiometric CIGS absorbers.<sup>[15]</sup>

In the double graded CIGS absorber typical of coevaporated layers, the so-called notch is the absorber region with lowest Ga content and associated bandgap. Engineering of the GGI  $[\text{Ga}]/([\text{Ga}]+[\text{In}])$  compositional gradient aims at increasing the notch width to maximize light absorption, while avoiding carriers collection issues arising from insufficient diffusion length and/or width of the space charge region. The final GGI gradient of coevaporated layers results from an interplay of competing processes, notably the preferential In diffusion to the surface during coevaporation and the In–Ga interdiffusion, which are affected by temperature, Cu concentration, presence of Cu<sub>x</sub>Se phases or of alkali. Experimental studies are notably reported in refs. [18–21] and references therein. An effective approach is

not yet fully mature to accurately predict GGI profiles from the deposition sequence under different growth conditions.<sup>[22]</sup>

## 1.2. Beneficial Effects of Alkali in CIGS

High-efficiency flexible CIGS generally use alkali-free substrates. The alkali elements can be effectively supplied by postdeposition treatment (PDT), consisting in the in situ evaporation of NaF at a reduced temperature in Se ambient. This incorporation strategy guarantees the absence of alkali during recrystallization. While this is no issue with high-temperature processes,<sup>[4]</sup> the presence of Na during recrystallization is problematic at low temperature as it affects the (In,Ga) interdiffusion, hinders grain growth,<sup>[23,24,19]</sup> and also impedes annihilation of stacking fault during the Cu-poor/Cu-rich transition,<sup>[25]</sup> notably impacting the carrier mobility at terahertz frequencies. This is probably the fundamental reason why PDT is the most effective method to supply Na in low-temperature CIGS.<sup>[26]</sup> Similarly, supply of heavy alkali elements during low-temperature CIGS deposition is also reported to generate defects and limit the cells performance.<sup>[27,28]</sup>

The PDT process was adapted to the heavier alkali compounds KF,<sup>[3]</sup> RbF, and CsF,<sup>[4,5]</sup> resulting in successive record efficiencies. Heavy-alkali PDT processes induce surface modifications enabling thinner CdS buffer layers, resulting in a gain in short-circuit current ( $J_{SC}$ ).<sup>[3]</sup> The open-circuit voltage ( $V_{OC}$ ) increase<sup>[29]</sup> associated with heavy alkali PDT occurs regardless of the choice of buffer layer (for example, Zn(O,S)<sup>[30]</sup>) and of the CIGS fabrication method (for example, sequential sputtering and selenization<sup>[31]</sup>). For high temperature processes, Jackson et al. report statistically better cell efficiencies with Rb and Cs as compared to K.<sup>[4]</sup> For low temperature processes, the different alkali act very similarly on the absorber.<sup>[32]</sup> Solar Frontier recently indicated absorber treatment with Cs (22.9% efficiency cells;<sup>[5]</sup> to our knowledge, the treatment of the current 23.35% efficiency record cell is not disclosed<sup>[6]</sup>). Handling of CsF is comparatively difficult due to its low vapor pressure and high hygroscopicity. Additionally, Rb may also be preferred to K as it can be better quantified by X-ray-based techniques in presence of In.

Alkali atoms segregate in large amounts at the CIGS grain boundaries.<sup>[33]</sup> Upon subsequent PDT with heavier alkali, Na gets substituted in integrated depth profiles (with K,<sup>[3]</sup> Rb, and Cs<sup>[4]</sup>), and Na concentration along grain boundaries significantly decreases.<sup>[33]</sup> Na is also found within the grains in concentrations of several tens ppm (experimental<sup>[34,35]</sup> and numerical<sup>[36]</sup> studies). In-grain solubility of heavy alkali is much lower<sup>[36]</sup> and the in-grain concentration is believed below APT detection limits.

The deposition of the CIGS absorber is commonly terminated with evaporation of a thin (In,Se) cap.<sup>[15,37–39]</sup> This is believed to lead to the formation of a Ga and Cu depleted surface and was found beneficial for device performance. Furthermore, PDT with heavy alkali is also known to promote Ga and Cu surface depletion<sup>[32,40]</sup> and to develop a different surface chemistry. Depending on process conditions, alkali–In–Se compounds form at the surface.<sup>[41]</sup> A layered RbInSe<sub>2</sub> compound was also observed at the CdS interface by TEM measurements.<sup>[42]</sup> First-principles simulations also predict very low



**Romain Carron** received the M.S. degree in physics from the Swiss Federal Institute of Technology in Lausanne (EPFL), Switzerland, and the Ph.D. degree in physics from EPFL in the field of quantum nanostructures for infrared light emission. After a stay in the industry he is since 2015 part of the Laboratory for Thin Films and Photovoltaics of

Prof. Ayodhya N. Tiwari at Empa, Switzerland. His research interests center on thin film photovoltaics and notably the CIGS technology, with a focus on absorbers and device fabrication, as well on optical, electrical, and material characterization.



**Shiro Nishiwaki** is a scientist in Laboratory for Thin Films & Photovoltaics at Empa. After receiving a Doctor in Engineering from Hokkaido University, Japan, he worked at Advanced Technology Research Laboratories of Matsushita Electric Co. Ltd, Japan, as a postdoctoral fellow of NEDO Industrial Technology Fellowship

Program from 1997 to 2000, at Hahn Meitner Institute, Germany as a guest scientist from 2000 to 2004, and at Institute of Energy Conversion, USA, as a limited term research associate from 2004 to 2007. His research interests focus on the material science for Cu chalcopyrite solar cells.



**Ayodhya N. Tiwari** is the Head of the Laboratory for Thin Films and Photovoltaics at Empa-Swiss Federal Laboratories for Materials Science and Technology in Dübendorf, Switzerland. His lab is involved in R&D of different types of thin film solar cells and holds the efficiency record for flexible CIGS solar cells. He is an adjunct

professor in the department of information technology and electrical engineering at ETH Zurich. He is the cofounder Zurich-based company Flisom involved in Roll-to-Roll manufacturing of monolithically connected lightweight flexible CIGS solar modules.

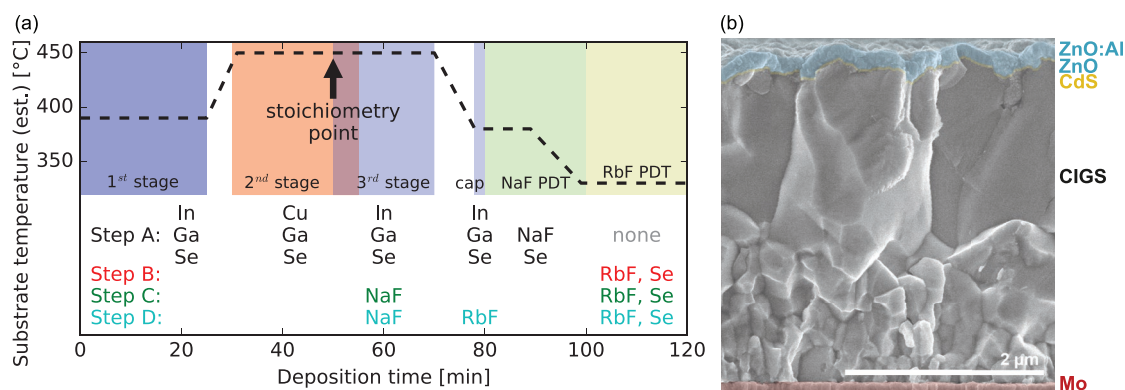


**Figure 1.** a) Typical CIGS deposition sequences of the baseline process A (black), as well as technological steps B (red), C (green), and D (cyan). The dashed line indicates the estimated actual substrate temperature. b) SEM cross-section of a typical finished solar cell evidencing the device structure.

solubilities of heavy alkali in the CIGS matrix, instead suggesting the formation of high-bandgap  $\text{AlInSe}_2$  compounds.<sup>[36]</sup>

As an alternative to the standard PDT procedure, the simultaneous evaporation of alkali during (In,Se) capping is also reported to positively affect  $V_{OC}$  and devices performance.<sup>[7,43]</sup>

### 1.3. This Work

In this contribution, we report in details the advances in CIGS absorber fabrication process achieved during the last years with our low temperature process on both PI and glass substrates. After description of the process improvement, we first demonstrate that a careful control of deposition conditions and elemental interdiffusion process enables growth of low-temperature absorbers with notch width as large as 1 μm. Starting from a baseline process with NaF PDT as only alkali supply, three technological improvements yield cells with successively increased efficiencies: RbF PDT treatment, NaF coevaporation during 3rd stage, and RbF coevaporation during cap deposition. In order to disentangle the effects of varying absorber bandgap, copper content, alkali incorporation method, and surface conditioning strategies, the  $V_{OC}$  and  $J_{SC}$  are analyzed in regards to their Shockley–Queisser limits corresponding to bandgap values deduced from external quantum efficiency (EQE) measurements. The effect of each technological step on the PV performance is quantified, and the causes of the improvements are discussed. The presence of alkali especially in the capping layer is also demonstrated to mitigate the detrimental apparent shunt limiting performance of near-stoichiometric absorbers.<sup>[16]</sup> Implementing the different process improvements, a CIGS cell grown on flexible PI with 20.8% efficiency was independently certified.

## 2. CIGS Deposition Process

CIGS absorber layers are deposited by multistage coevaporation at substrate temperature around 450 °C on flexible polyimide and soda-lime glass (SLG) with alkali diffusion barrier, after Mo coating (DC sputtering). SLG and PI substrates are placed side-by-side in the reactor. Solar cells were completed with chemical bath deposition of CdS (around 20 nm), RF

sputtering of nonintentionally doped ZnO (around 60 nm) and ZnO:Al (around 120 nm) layers, and e-beam evaporation of Ni–Al grids. In a few cases specified in this paper, a  $\text{MgF}_2$  antireflection coating was deposited by e-beam evaporation. Figure 1b shows the SEM cross-section of a typical finished cell. Further information about the reactor and the process can be found in ref. [44].

The baseline process hereafter referred to “A” is depicted in Figure 1a and typically yields cells with efficiency slightly above 18%. The deposition starts with evaporation of a (In, Ga, Se) 1st stage followed by a (Cu, Ga, Se) 2nd stage. In evaporation resumes when stoichiometry point is reached. The duration of the excess Cu evaporation determines the final CGI content as well as the notch width. After 3rd stage the CGI composition is below unity and the substrate temperature is decreased. A (In, Ga, Se) cap with thickness around 50 nm is evaporated prior to NaF PDT. In this baseline process “A” only a NaF PDT is applied.

Technological step “B” introduces a RbF PDT performed sequentially after NaF PDT, similarly as the KF PDT described in ref. [3]. Step “C” consists in the evaporation of NaF in addition to In and Ga starting from the stoichiometry point, in an amount equivalent to around 5 nm. Finally, technological step “D” aims at altering the CIGS surface by coevaporation of RbF during the (In,Ga,Se) cap deposition prior to PDT. The RbF amount is below 1/10th of that evaporated during PDT. For steps B, C, and D, surface modifications associated with RbF PDT enable a thinning of the CdS buffer layer from around 50 nm to around 30 nm.

Out of the depositions performed in the growth chamber, around 220 runs corresponding to around 380 samples on PI or SLG substrates are categorized in these four technological steps and discussed in this study. Each sample consists in up to 18 cells. Fabrication of samples of previous technological steps continued even after introduction of improved processes, yielding cells with properties in line with earlier results.

## 3. Results

### 3.1. GGI Notch Engineering

A challenge of low-temperature CIGS is the engineering of the GGI gradient. A wide bandgap minimum is desired to increase

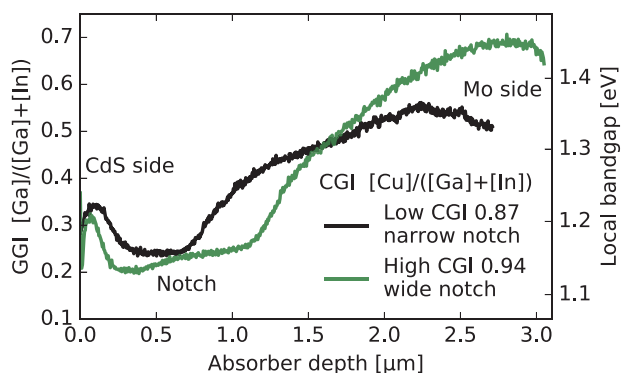


**Figure 2.** GGI depth profiles extracted from SIMS data, for samples with low (0.87) and high (0.94) CGI. The right axis shows the corresponding local bandgap, following the dependency given in ref. [13]. The notch width can be tuned from around 500 nm up to almost 1  $\mu\text{m}$ .

the optical absorption without compromising the  $V_{\text{OC}}$ . In this work, the CGI was tuned by adjusting the duration of the excess Cu evaporation after the stoichiometry point. Combined with an adjustment of the evaporation rates of Ga and In during the Cu-rich phase, this enables the formation of a wide region with almost constant GGI composition. Examples of GGI depth profiles are shown in **Figure 2**, for two samples with very different Cu excess processes: the depth of the nearly flat notch region can be increased from around 500 nm for baseline process to almost 1  $\mu\text{m}$ , resulting in a significant  $J_{\text{SC}}$  increase as described below.

### 3.2. Efficiency Improvement

**Figure 3** reports the sample power conversion efficiency for the four technological steps investigated in this study. The efficiency of each sample corresponds to the average of up to 18 individual cells measured without antireflection coating. Samples produced on PI and SLG substrates are reported in almost equal numbers. The nature of the substrate has no influence on device efficiency (difference less than 0.2% absolute on average, possibly due to scribing). Additionally, EQE

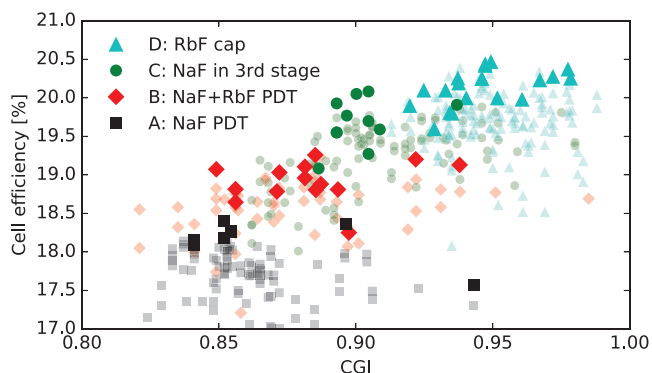


**Figure 3.** Cells efficiency as function of the absorber CGI, for the four investigated technological steps (without ARC). Small symbols refer to sample averages (up to 18 cells). The large symbols show individual cells characterized in more details in sections 3.3 and 3.4.

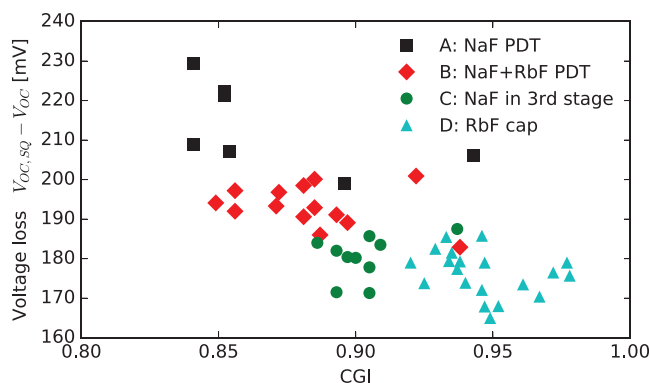


**Figure 4.**  $V_{\text{OC}}$  deficit to the Shockley-Queisser limit as a function of the absorber CGI.

measurements were performed on a selection of cells which efficiency is evidenced using large symbols. Each of the technological step B, C, and D leads to increased efficiency as compared to the previous step. The CGI composition yielding the highest efficiencies also increases with each of the technological steps.

The increase in the PV performance essentially results from increases in  $V_{\text{OC}}$  and  $J_{\text{SC}}$ , while most other PV parameters remain almost unchanged (FF, ideality factor,  $J_0$  or series resistance as shown in Figure S2, Supporting Information). To understand the clear statistical increase in efficiency and lift the ambiguity caused by sample-to-sample bandgap variations, the optical bandgap of a few individual cells was extracted from EQE measurements using the inflection point method.<sup>[45]</sup> In the following, for each of these cells the  $V_{\text{OC}}$  and  $J_{\text{SC}}$  are compared to the Shockley-Queisser limits  $V_{\text{OC},\text{sq}}$  and  $J_{\text{SC},\text{sq}}$  obtained from the optical bandgap (tabulated values available in ref. [46]). With this analysis, we aim at distinguishing the influence of alkali incorporation method from that of the increased CGI.

### 3.3. Effect of Alkali Incorporation and CGI on $V_{\text{OC}}$

**Figure 4** shows the  $V_{\text{OC}}$  deficit  $V_{\text{OC},\text{sq}} - V_{\text{OC}}$  as a function of the absorber CGI. For a given CGI, RbF PDT appears to yield a  $V_{\text{OC}}$  gain of around 15–20 meV, similarly as observed with KF.<sup>[29]</sup> Addition of Na in the 3rd stage increases  $V_{\text{OC}}$  by a further  $\approx 15$  meV for comparable CGI. By contrast, RbF evaporation during cap deposition only marginally affects the  $V_{\text{OC}}$ . Considering each processing step independently, the  $V_{\text{OC}}$  improvement appears primarily driven by the alkali incorporation method, and the effect of varying CGI appears marginal.

One of the limitations to the  $V_{\text{OC}}$  is the presence of spatial and temporal potential fluctuations in the absorber bandgap,<sup>[47]</sup> which can be quantified using the Urbach energy. Empirical comparison of several PV technologies suggest a strong link between these quantities,<sup>[47]</sup> but the underlying mechanism remains unclear. **Figure 5** displays the Urbach energy as function of the absorber CGI for the different technological steps, determined by exponential absorption tail in the long-wavelength edge of the EQE. Due to the fitting range close to the bandgap (typically between 0.1% and 3% EQE values), the



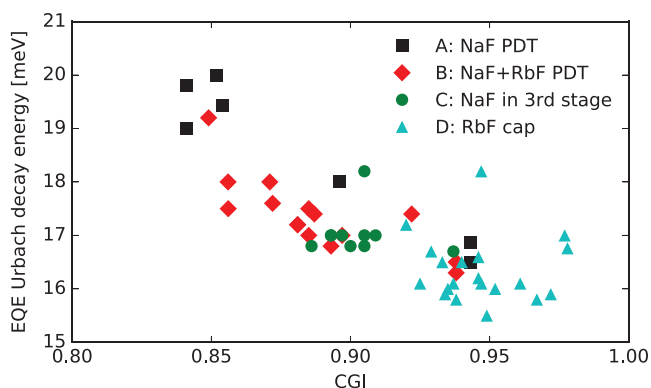


**Figure 5.** Urbach energies determined from EQE as a function of the absorber CGI.

values are slightly larger than the ones determined from PL.<sup>[48]</sup> For each of the technological step, the Urbach energy decreases with increasing CGI. No clear difference appears between steps B, C, and D: increasing the CGI close to stoichiometry very effectively reduces the magnitude of potential fluctuations, in line with existing reports.<sup>[11]</sup> Conversely, a negligible impact on the potential fluctuations is provided by Na supply during 3rd stage, and by Rb coevaporation in the cap. The sample series A (NaF PDT) exhibit decay energies higher by around 1 meV as compared to series B, C, and D: the RbF PDT effectively reduces the magnitude of the potential fluctuations in the absorber, which in this case can be linked to a 15–20 mV  $V_{OC}$  increase.<sup>[48]</sup>

Increasing the CGI effectively reduces the magnitude of potential fluctuations. However, we do not evidence a clear and unambiguous correlation of the Urbach energy with  $V_{OC}$  deficit as other factors also influence the  $V_{OC}$ . As an example, the samples of series A that exhibit low values of the Urbach energy suffer from large  $V_{OC}$  deficits. Also, samples of series D present Urbach energies clearly lower than series C, but almost similar  $V_{OC}$  deficits. The moderate gain in  $V_{OC}$  with decreased Urbach energy is also below expectations of the empiric trend evidenced in ref. [47]. Notably, the notch width also plays a role in the  $V_{OC}$  deficit. A wide notch provides more space to accommodate charges therefore reduces the electron density, decreases the electron quasi-Fermi level and the  $V_{OC}$ . With our process, the wider notch that comes together with the increased CGI may offset part of the expected  $V_{OC}$  gains.

### 3.4. Effect of CGI on $J_{SC}$

In order to separate the influence of optical absorption and varying bandgap, we compute the  $J_{SC}$  deficit as the difference between experimental  $J_{SC,EQE}$  obtained from integration of the EQE (without antireflective coating ARC) with the Shockley–Queisser

value  $J_{SC,SQ}$  corresponding to the absorber bandgap determined above. As shown in **Figure 6a**, the  $J_{SC}$  deficit decreases for increasing CGI. In the figure,  $J_{SC}$  deficits of series A samples (NaF PDT, open symbols) were decreased by  $0.8 \text{ mA cm}^{-2}$  to account for the systematically thicker CdS layer in these cells. In this graph only the lower values are relevant, as poor PV parameters can originate from multiple external factors. In the following, we first demonstrate that the immediate cause for the improved  $J_{SC}$  is an increased spectral response in the near-infrared, which we then assign to an increased CGI composition and to a widened notch.

We characterize the steepness of the near-infrared spectral response with the slope in the linear portion of the Tauc plot ( $E \text{ EQE}$ )<sup>2</sup> versus  $E$  near the bandgap energy. The  $J_{SC}$  deficit displayed in **Figure 6b** decreases with increased slope. No clear difference is observed between the different samples series. To understand the observed evolution, we performed optical TMM simulations assuming perfect collection as detailed in refs. [13] and [45]. Simulation series were conducted by varying the CGI composition on four different GGI grading profiles with various notch widths. The different GGI gradings and some selected simulated EQE curves are shown in **Figure S1** of the Supporting Information. The CGI affects the absorption coefficient as described in ref. [13]. The  $J_{SC}$  deficit was extracted following the same procedure with simulated EQE as with experimental curves. The  $J_{SC}$  deficits of simulated EQE are independent of the specific GGI grading, and follow the same trend as the experimental data in **Figure 6b**. The slightly larger values are consistent with the comparatively higher simulated reflectances as compared to experimental curves caused by improved light coupling at rough interfaces, as already reported in ref. [13]. With this comparison, we assign the improved  $J_{SC}$  to an improved spectral response in the near infrared and we discard alternatives such as a reduced carrier collection, modified reflectance or absorption in the window layers.

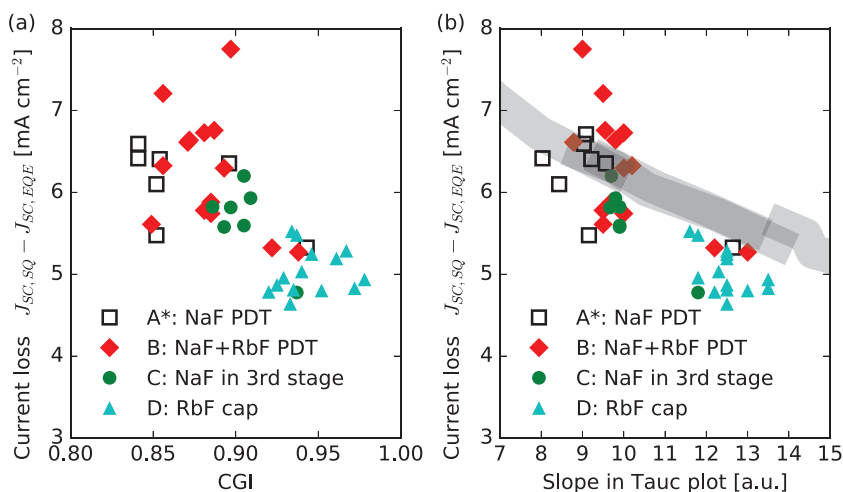


**Figure 6.** a)  $J_{SC}$  deficit to the Shockley–Queisser value as function of the absorber CGI.  $J_{SC}$  deficits of series A\* (open symbols) are decreased by  $0.8 \text{ mA cm}^{-2}$  to account for the systematically thicker CdS layer in NaF treated samples. b)  $J_{SC}$  deficit as function of the slope in the Tauc plot ( $E \text{ EQE}$ )<sup>2</sup> versus  $E$ . Thick stripes show  $J_{SC}$  deficits of simulations with various CGI and GGI grading shapes.

Comparison of experimental and simulation data reveals that the CGI-dependent optical absorption coefficient (see ref. [13]) only partially explains the improved spectral response. An increased notch width is therefore necessary to explain the improved infrared spectral response at high CGI visible in Figure 6a and the corresponding improved  $J_{SC}$  values. However, with the deposition sequence CGI and notch width are difficult to modify independently and a direct experimental confirmation could not be obtained.

### 3.5. Fill Factor and Apparent Cell Shunt

Experimental current–voltage ( $J$ – $V$ ) curves generally follow a linear behavior around  $V = 0$ , quantified with the apparent parallel resistance  $R_p$ . PV performance significantly degrades below a few thousand  $\Omega \text{ cm}^2$  essentially through a fill factor (FF) reduction. Absorbers with CGI approaching unity typically present low  $R_p$  values,<sup>[16]</sup> which is the main restriction for using high CGI compositions. We consider a  $R_p$  value of  $1500 \Omega \text{ cm}^2$  as an (arbitrary) lowest acceptable value as it results in around 0.25% absolute efficiency loss (see Figure 7b where a 1-diode model is implemented with 1 resistor,  $36 \text{ mA cm}^{-2} J_{SC}$ , 1.5 ideality factor,  $3 \times 10^{-7} \text{ mA cm}^{-2} J_0$ ).

Figure 7a shows the apparent shunt  $R_p$  measured under 1-sun illumination as function of the absorber CGI (for each sample, the median value of up to 18 cells is reported). For series A, B, and C a clear downward trend is visible with increasing CGI, yielding  $R_p$  values mostly below  $1500 \Omega \text{ cm}^2$  for CGI ratios above 0.9. Technological steps A and B behave similarly, while step C presents slightly improved  $R_p$  values at high CGI compositions. Only with step D (capping with RbF) it was possible to produce cells with CGI approaching stoichiometry, while maintaining values of the parallel resistance on average clearly above  $1500 \Omega \text{ cm}^2$ .

The cause for the  $R_p$  degradation at high CGI is controversial. The generally higher values measured in the dark suggests that  $R_p$  originates from voltage-dependent carrier collection.

However, we generally observe a correlation of  $R_p$  values in dark and illuminated conditions, hinting that an actual shunt path is primarily responsible for the performance degradation. Possible interpretations are the formation of additional vertical shunt paths, the increased density or the increased activity of these at high CGI. Virtuani et al.<sup>[16]</sup> mention percolation along grain boundaries as a possible model, but instead favored “hot-spots” at localized recombination centers such as crevices, voids or interface defects. The improved lateral conductivity of CIGS with high CGI may also worsen the effect of existing localized shunt centers. The improved shunt behavior of step D as well as literature results<sup>[15]</sup> suggest the primary cause lies at the top-most CIGS layer or at the interface with the buffer layer.

### 3.6. Champion Flexible Solar Cell

Implementing the improved deposition process D and after deposition of a  $\text{MgF}_2$  antireflection coating, a champion device on PI substrate was independently certified, yielding a new record for CIGS on flexible substrate of 20.8% power conversion efficiency. The photovoltaic parameters of this cell are reported in Table 1, and  $J$ – $V$  and EQE curves are displayed in Figure 8. The absorber integral composition is GGI 0.41 and CGI 0.98 (X-ray fluorescence (XRF) values), and the window layers consist of around 20 nm CdS, 65 nm ZnO, and 110 nm ZnO:Al. The previous best cell is classified under technological step “B,” and was grown in a different reactor with significant discrepancies in the deposition sequence.

## 4. Conclusion

As a summary, we introduced three successive process improvements to our low temperature CIGS deposition sequence on both polyimide and glass substrates. Each improved process yielded cells with increased PV performance, achieving reliable manufacturing of cells with efficiency above 20%. A cell with 20.8% efficiency was independently certified by Fraunhofer ISE, yielding a new record for CIGS on flexible substrate.

The improvement in PV performance is discussed in terms of  $V_{OC}$  and  $J_{SC}$  deficit to the Shockley–Queisser limit. In line with previous reports, introduction of heavy alkali PDT (here RbF) increases  $J_{SC}$  due to lesser parasitic absorption in a thinner CdS layer while improving simultaneously  $V_{OC}$  by about 15–20 mV, which we associate with a reduction in the Urbach energy by about 1 meV. PDT with heavy alkali reduces the amplitude of potential fluctuations in the bulk, especially close to grain boundaries and crystallographic defects. Coevaporation of NaF after recrystallization allows for larger CGI absorber compositions and increases  $V_{OC}$ . The underlying mechanisms seems unrelated to potential fluctuations

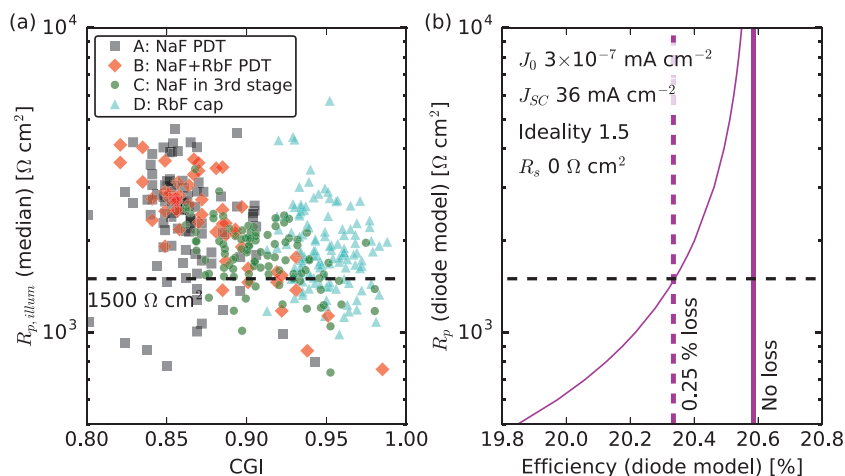


**Figure 7.** a)  $R_{p,illum}$  (median value for each sample) as function of the absorber CGI. Using process D, acceptable values of the parallel resistance are obtained even with near-stoichiometric absorbers. b) Efficiency computed with a diode model, evidencing the efficiency loss associated with a parallel resistance  $R_p$  of  $1500 \Omega \text{ cm}^2$ .

**Table 1.** Photovoltaic parameters of a 20.8% efficient CIGS cell on flexible PI substrate (with ARC), independently certified at Fraunhofer ISE. The previous best cell on flexible is also shown for comparison.

	$V_{OC}$ [mV]	$J_{SC}$ [mA cm <sup>-2</sup> ]	FF [%]	Efficiency [%]	Area [cm <sup>2</sup> ]
CIGS on PI	734.4 ± 2.5	36.74 ± 0.70	77.17 ± 0.50	20.82 ± 0.42	0.5149 ± 0.0032
Previous certified best <sup>[3]</sup>	736	35.1	78.9	20.4	0.52

and deserves further investigations. Finally, coevaporation of RbF in the (In, Ga, Se) capping layer enables further  $J_{SC}$  and efficiency improvements via increased absorber CGI and notch width. This treatment also mitigates the adverse shunting typically associated with high CGI compositions, evidencing the critical role of surface layer preparation for near-stoichiometric absorbers.

The benefit of an increased CGI on the PV performance is threefold. First, the absorber crystal quality is improved, assessed by a strong decrease in the Urbach energy. Second, the increased optical absorption in the CIGS improves the  $J_{SC}$ . Finally, we take advantage of the increased CGI to widen to about 1  $\mu$ m the notch region where the bandgap is minimum, thus increasing the spectral response in the infrared.  $V_{OC}$  improvements are observed strongly connected to the alkali supply strategy, and more weakly to the CGI and potential fluctuations.

Cell efficiencies of low-temperature process are below the efficiency of CIGS on glass substrates, mostly in reason of inferior  $V_{OC}$  and FF. Compared with absorbers grown at higher temperatures (>550 °C), our material suffers from higher level of disorder as evidenced with Urbach energies measured by PL.<sup>[48]</sup> The low doping level of our absorbers (below 1E16 cm<sup>-3</sup> estimated from C–V profiling) is also a limit for reaching higher  $V_{OC}$  and efficiencies. Finally, we did not observe the

improvement in the diode ideality factor upon heavy alkali treatment, suggested in ref. [4] as the main benefit of heavy alkali PDT. Closing the gap of our poor values of FF and diode ideality factor is a major challenge of our low-temperature CIGS deposition route.

## 5. Experimental Section

Integral composition was determined after CIGS deposition by fitting of the  $K\alpha$  peaks of Cu, In, Ga, and Se in XRF measurements (45 keV home-built setup). The repeatability confidence interval on the CGI composition is about 2.7% (2 $\sigma$ ). The reported CGI values are believed to be underestimated the real compositions, by less than 0.03. Finished devices are characterized by current–voltage ( $I$ – $V$ ) analysis at 25 °C in 4-probe configuration with a simulated AM1.5G spectrum in an ABA-class solar simulator. The EQE spectra are recorded by illuminating the cell with a chopped monochromatic light produced by a white light halogen lamp and an LOT MSH-300 monochromator, under around 0.2 sun halogen bias light. The measured current is calibrated against a certified Si cell and a calibrated Ge cell, yielding EQE data with 3 to 3.5 orders of magnitude. Temperature dependent capacitance measurements are carried out in a home-built liquid nitrogen cooled cryostat. Compositional depth profile were acquired using time-of-flight secondary ion mass spectrometry (ION-TOF GmbH TOF SIMS5) with O<sub>2</sub><sup>+</sup> for sputtering and Bi<sup>+</sup> for analyzing.

## Supporting Information

Supporting Information is available from the Wiley Online Library or from the author.

## Acknowledgements

R.C. and S.N. contributed equally to this work. This work received funding from European Union's Horizon 2020 research and innovation programme under Grant Agreement No. 641004 ("Sharc25"), of the Swiss State Secretariat for Education, Research and Innovation (SERI SBFI) under Contract No. 15.0158, of the Swiss Federal Office of Energy (SFOE) (SI/501614-01 "ImproCIS"), and of the Swiss National Science Foundation (SNSF) under Grant No. 407040-153916 ("PV2050"). This article was published as part of the *Advanced Energy Materials* Excellence in Energy special series.

## Conflict of Interest

The authors declare no conflict of interest.

## Keywords

alkali, CIGS, Cu(In,Ga)Se<sub>2</sub>, flexible, PDT

Received: February 1, 2019

Revised: April 4, 2019

Published online: May 8, 2019

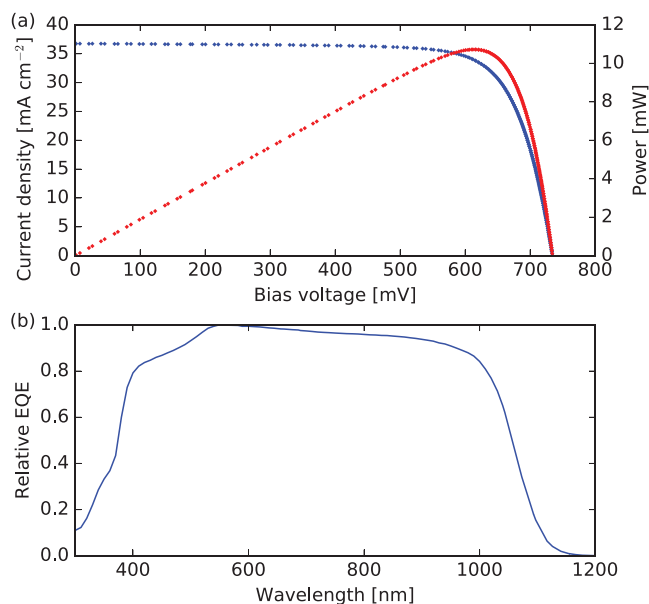


**Figure 8.**  $J$ – $V$  and normalized EQE curves of the best independently certified solar cell on PI substrate.

- [1] T. Feurer, P. Reinhard, E. Avancini, B. Bissig, J. Lockinger, P. Fuchs, R. Carron, T. P. Weiss, J. Perrenoud, S. Stutterheim, S. Buecheler, A. N. Tiwari, *Prog. Photovoltaics* **2017**, *25*, 645.

- [2] M. O. Reese, S. Glynn, M. D. Kempe, D. L. McGott, M. S. Dabney, T. M. Barnes, S. Booth, D. Feldman, N. M. Haegel, *Nat. Energy* **2018**, 3, 1002.
- [3] A. Chirila, P. Reinhard, F. Pianezzi, P. Bloesch, A. R. Uhl, C. Fella, L. Kranz, D. Keller, C. Gretener, H. Hagendorfer, D. Jaeger, R. Erni, S. Nishiwaki, S. Buecheler, A. N. Tiwari, *Nat. Mater.* **2013**, 12, 1107.
- [4] P. Jackson, R. Wuerz, D. Hariskos, E. Lotter, W. Witte, M. Powalla, *Phys. Status Solidi RRL* **2016**, 10, 583.
- [5] T. Kato, J. L. Wu, Y. Hirai, H. Sugimoto, V. Bermudez, *IEEE J. Photovoltaics* **2019**, 9, 325.
- [6] Solar Frontier Achieves World Record Thin-Film Solar Cell Efficiency of 23.35%, [http://www.solar-frontier.com/eng/news/2019/0117\\_press.html](http://www.solar-frontier.com/eng/news/2019/0117_press.html) (accessed: January 2019).
- [7] M. Balestrieri, V. Achard, T. Hildebrandt, L. Lombez, M. Jubault, S. Bechu, M. Bouttemy, A. Etcheberry, D. Lincot, F. Donsanti, *IEEE J. Photovoltaics* **2018**, 8, 1343.
- [8] P. Jackson, D. Hariskos, E. Lotter, S. Paetel, R. Wuerz, R. Menner, W. Wischmann, M. Powalla, *Prog. Photovoltaics* **2011**, 19, 894.
- [9] S. B. Zhang, S. H. Wei, A. Zunger, H. Katayama-Yoshida, *Phys. Rev. B* **1998**, 57, 9642.
- [10] C. Persson, A. Zunger, *Phys. Rev. Lett.* **2003**, 91, 266401.
- [11] S. Siebentritt, L. Gutay, D. Regesch, Y. Aida, V. Depredurand, *Sol. Energy Mater. Sol. Cells* **2013**, 119, 18.
- [12] E. Avancini, R. Carron, B. Bissig, P. Reinhard, R. Menozzi, G. Sozzi, S. Di Napoli, T. Feurer, S. Nishiwaki, S. Buecheler, A. N. Tiwari, *Prog. Photovoltaics* **2017**, 25, 233.
- [13] R. Carron, E. Avancini, T. Feurer, B. Bissig, P. A. Losio, R. Figi, C. Schreiner, M. Bürki, E. Bourgeois, Z. Remes, M. Nesladek, S. Buecheler, A. N. Tiwari, *Sci. Technol. Adv. Mater.* **2018**, 19, 396.
- [14] W. Witte, R. Kniese, M. Powalla, *Thin Solid Films* **2008**, 517, 867.
- [15] Y. Aida, V. Depredurand, J. K. Larsen, H. Arai, D. Tanaka, M. Kurihara, S. Siebentritt, *Prog. Photovoltaics* **2015**, 23, 754.
- [16] A. Virtuani, E. Lotter, M. Powalla, U. Rau, J. H. Werner, M. Acciarri, *J. Appl. Phys.* **2006**, 99, 014906.
- [17] P. Jackson, R. Wurz, U. Rau, J. Mattheis, M. Kurth, T. Schlotzer, G. Bilger, J. H. Werner, *Prog. Photovoltaics* **2007**, 15, 507.
- [18] A. M. Gabor, J. R. Tuttle, M. H. Bode, A. Franz, A. L. Tennant, M. A. Contreras, R. Noufi, D. G. Jensen, A. M. Hermann, *Sol. Energy Mater. Sol. Cells* **1996**, 41–42, 247.
- [19] O. Lundberg, J. Lu, A. Rockett, M. Edoff, L. Stolt, *J. Phys. Chem. Solids* **2003**, 64, 1499.
- [20] A. Chirila, S. Buecheler, F. Pianezzi, P. Bloesch, C. Gretener, A. R. Uhl, C. Fella, L. Kranz, J. Perrenoud, S. Seyrling, R. Verma, S. Nishiwaki, Y. E. Romanyuk, G. Bilger, A. N. Tiwari, *Nat. Mater.* **2011**, 10, 857.
- [21] V. Achard, M. Balestrieri, S. Bechu, M. Jubault, M. Bouttemy, L. Lombez, T. Hildebrandt, N. Naghavi, A. Etcheberry, D. Lincot, F. Donsanti, *Thin Solid Films* **2019**, 669, 494.
- [22] I. L. Repins, S. Harvey, K. Bowers, S. Glynn, L. M. Mansfield, *MRS Adv.* **2017**, 2, 3169.
- [23] R. Caballero, C. A. Kaufmann, T. Eisenbarth, M. Cancela, R. Hesse, T. Unold, A. Eicke, R. Klenk, H. W. Schock, *Thin Solid Films* **2009**, 517, 2187.
- [24] D. Rudmann, M. Kaelin, F. J. Haug, F. Kurdesau, H. Zogg, A. N. Tiwari, *Proc. 3rd World Conf. on Photovoltaic Energy Conversion*, Vols A–C, IEEE, Osaka, Japan **2003**, p. 376.
- [25] H. Stange, S. Brunken, H. Hempel, H. Rodriguez-Alvarez, N. Schafer, D. Greiner, A. Scheu, J. Lauche, C. A. Kaufmann, T. Unold, D. Abou-Ras, R. Mainz, *Appl. Phys. Lett.* **2015**, 107, 152103.
- [26] D. Rudmann, D. Bremaud, A. F. da Cunha, G. Bilger, A. Strohm, M. Kaelin, H. Zogg, A. Tiwari, *Thin Solid Films* **2005**, 480, 55.
- [27] F. Pianezzi, P. Reinhard, A. Chirila, S. Nishiwaki, B. Bissig, S. Buecheler, A. N. Tiwari, *J. Appl. Phys.* **2013**, 114, 194508.
- [28] F. Pianezzi, P. Reinhard, A. Chirila, B. Bissig, S. Nishiwaki, S. Buecheler, A. N. Tiwari, *Phys. Chem. Chem. Phys.* **2014**, 16, 8843.
- [29] P. Reinhard, F. Pianezzi, B. Bissig, A. Chirila, P. Blosch, S. Nishiwaki, S. Buecheler, A. N. Tiwari, *IEEE J. Photovoltaics* **2015**, 5, 656.
- [30] T. M. Friedlmeier, P. Jackson, A. Bauer, D. Hariskos, O. Kiowski, R. Wuerz, M. Powalla, *IEEE J. Photovoltaics* **2015**, 5, 1487.
- [31] L. M. Mansfield, R. Noufi, C. P. Muzzillo, C. DeHart, K. Bowers, B. To, J. W. Pankow, R. C. Reedy, K. Ramanathan, *IEEE J. Photovoltaics* **2014**, 4, 1650.
- [32] E. Avancini, R. Carron, T. P. Weiss, C. Andres, M. Burki, C. Schreiner, R. Figi, Y. E. Romanyuk, S. Buecheler, A. N. Tiwari, *Chem. Mater.* **2017**, 29, 9695.
- [33] A. Vilalta-Clemente, M. Raghuwanshi, S. Duguay, C. Castro, E. Cadel, P. Pareige, P. Jackson, R. Wuerz, D. Hariskos, W. Witte, *Appl. Phys. Lett.* **2018**, 112, 103105.
- [34] O. Cococar-Miredin, T. Schwarz, P. P. Choi, M. Herbig, R. Wuerz, D. Raabe, *JoVE-J. Visualized Exp.* **2013**, 74, e50376.
- [35] F. Couzinie-Devy, E. Cadel, N. Barreau, L. Arzel, P. Pareige, *Appl. Phys. Lett.* **2011**, 99, 232108.
- [36] M. Malitckaya, H. P. Komsa, V. Havu, M. J. Puska, *J. Phys. Chem. C* **2017**, 121, 15516.
- [37] J. A. AbuShama, S. W. Johnston, D. L. Young, R. Noufi, *Thin-Film Comp. Semicond. Photovoltaics* **2005**, 865, 335.
- [38] I. Repins, M. A. Contreras, B. Egaas, C. DeHart, J. Scharf, C. L. Perkins, B. To, R. Noufi, *Prog. Photovoltaics* **2008**, 16, 235.
- [39] I. Khatri, M. Sugiyama, T. Nakada, *Prog. Photovoltaics* **2017**, 25, 871.
- [40] F. Babbe, H. Elanzeery, M. Melchiorre, A. Zelenina, S. Siebentritt, *Phys. Rev. Mater.* **2018**, 2, 105405.
- [41] P. Reinhard, B. Bissig, F. Pianezzi, H. Hagendorfer, G. Sozzi, R. Menozzi, C. Gretener, S. Nishiwaki, S. Buecheler, A. N. Tiwari, *Nano Lett.* **2015**, 15, 3334.
- [42] N. Taguchi, S. Tanaka, S. Ishizuka, *Appl. Phys. Lett.* **2018**, 113, 113903.
- [43] T. Lepetit, S. Harel, L. Arzel, G. Ouvrard, N. Barreau, *IEEE J. Photovoltaics* **2016**, 6, 1316.
- [44] S. Nishiwaki, T. Feurer, B. Bissig, E. Avancini, R. Carron, S. Buecheler, A. N. Tiwari, *Thin Solid Films* **2017**, 633, 18.
- [45] R. Carron, C. Andres, E. Avancini, T. Feurer, S. Nishiwaki, S. Pisoni, F. Fu, M. Lingg, Y. E. Romanyuk, S. Buecheler, A. N. Tiwari, *Thin Solid Films* **2019**, 669, 482.
- [46] S. Ruhle, *Sol. Energy* **2016**, 130, 139.
- [47] S. De Wolf, J. Holovsky, S. J. Moon, P. Loper, B. Niesen, M. Ledinsky, F. J. Haug, J. H. Yum, C. Ballif, *J. Phys. Chem. Lett.* **2014**, 5, 1035.
- [48] M. H. Wolter, R. Carron, E. Avancini, B. Bissig, T. P. Weiss, T. Feurer, S. Nishiwaki, S. Buecheler, E. Bourgeois, G. Degutis, P. Jackson, W. Witte, S. Siebentritt, unpublished.